

Data Compression with ENO Schemes: A Case Study¹

Sergio Amat² and Francesc Aràndiga²

Departament de Matemàtica Aplicada, Universitat de València, València, Spain
E-mail: arandiga@uv.es

Albert Cohen

Laboratoire d'Analyse Numerique, Université Pierre et Marie Curie, Paris, France

Rosa Donat² and Gregori Garcia

Departament de Matemàtica Aplicada, Universitat de València, València, Spain

and

Markus von Oehsen³

Institut für Mathematik, Medizinische Universität zu Lübeck, 23564 Lübeck, Germany

Communicated by Charles K. Chui.

Received July 21, 2000

We study the compression properties of ENO-type nonlinear multiresolution transformations on digital images. Specific error control algorithms are used to ensure a prescribed accuracy. The numerical results reveal that these methods strongly outperform the more classical wavelet decompositions in the case of piecewise smooth geometric images. © 2001 Academic Press

1. INTRODUCTION

Multiresolution representations, combined with appropriate quantization algorithms such as those in [16] and [17], are currently one of the most efficient tools for image data compression. The interpretation of these representations in terms of decompositions into wavelet bases provides a mathematical framework which allows us to analyze the performance of such compression algorithms.

¹ Research supported in part by TMR Project ERBFMRX-CT98-0184.

² Research supported in part by DGICYT PB97-1402.

³ Supported by a grant of the Graduiertenkolleg 357, DFG.

The starting point to this analysis is *nonlinear approximation*: a signal f is “compressed” by its partial expansion f_N in the wavelet basis, which retains only the N largest contributions in some prescribed metric X . The most commonly used metric for thresholding images is $X = L^2$ but many other norms can be considered. It is then possible to completely characterize those functions such that $\sigma_N(f) = \|f - f_N\|_X$ behaves as $\mathcal{O}(N^{-r})$ for a given r (see, e.g., [8] for a survey on such results). Of course, the compression algorithms that we have in mind are more complicated than such simple thresholding procedures, since they should result in an approximation \tilde{f}_N which can be encoded on a finite number of bits N . However, it was recently observed (see [4, 6, 9]) that at low bit rate, the compression error $\varepsilon(N) = \|f - \tilde{f}_N\|_X$ produced by algorithms of the type in [16] or [17] behaves essentially like the nonlinear approximation error $\sigma_N(f)$.

Therefore, the performance of nonlinear approximation by thresholding procedures can be viewed as a good indicator of the compression capabilities of a given basis. In the practice of real images, *edges* constitute the main limitation to efficient nonlinear approximation, since the numerically significant coefficients at fine scales are essentially those for which the wavelet support is intersected by such discontinuities. In particular, this limits the efficiency of high-order wavelets due to their large supports.

The goal of this case study is to examine the compression properties of a class of high-order multiresolution decompositions, introduced by Harten in the late 1980s and early 1990s in the context of numerical shock computations, which perform a specific adaptive treatment of edges. An important feature of these decompositions is that they are nonlinearly data dependent and therefore cannot be exactly thought of as an expansion into a wavelet basis.

The rest of the material is organized as follows. In Section 2, we briefly recall these decompositions and their relations to wavelet bases, in the context of cell-average discretizations which seem well-fitted for images. The data-dependent nature of these decompositions introduces new difficulties when it comes to thresholding procedures. We present in Section 3 a specific error control strategy that deals with these difficulties. Numerical results on test images, based on tensor product decompositions, are presented in Section 4. We can roughly summarize these results as follows: nonlinear decompositions outperform standard wavelet decompositions in the case of synthetic geometric images, which are smooth except along curved discontinuities, but they do not bring significant improvements for real images which contain additional texture. This raises the perspective of separating the geometric and textural information in an image in order to benefit from these new decompositions.

2. LINEAR AND NONLINEAR DECOMPOSITIONS

There exist many different approaches to multiresolution decompositions, which are closely connected: wavelet bases, subband filtering, and hierarchical splitting of finite element spaces. Here, it will be convenient to use the discrete framework of Harten, based on *decimation and prediction*, which we briefly recall below (more details can be found in [2] or [14]).

From a set of discrete data $f^k = (f_i^k)_{i=1,\dots,N_k}$, where k represents the level of discretization, the *decimation operator* D_k^{k-1} computes $f^{k-1} = (f_i^{k-1})_{i=1,\dots,N_{k-1}}$ at the next coarser level of discretization ($N_{k-1} < N_k$). The *prediction operator* P_{k-1}^k maps

a coarse vector f^{k-1} onto a finer one $\tilde{f}^k = (\tilde{f}_i^k)_{i=1,\dots,N_k}$, which should be thought as an approximation of f^k . In contrast to decimation, the prediction operator need not be linear, but should at least satisfy the consistency requirement $D_k^{k-1} P_{k-1}^k = I_{N_{k-1}}$. It follows that the image of D_k^{k-1} operator is the full $\mathbf{R}^{N_{k-1}}$, so that *detail space* W_{k-1} defined as the null space of P_k^{k-1} has dimension $N_k - N_{k-1}$. If $(e_i^{k-1})_{i=1,\dots,N_k-N_{k-1}}$ is a basis of W_k , we can decompose the *prediction error* according to

$$f^k - \tilde{f}^k = \sum_{i=1,\dots,N_k-N_{k-1}} d_i^{k-1} e_i^{k-1}. \quad (2.1)$$

Therefore, we can represent f^k by (f^{k-1}, d^{k-1}) , where $d^{k-1} = (d_i^{k-1})_{i=1,\dots,N_k-N_{k-1}}$. By iteration of this process from $k = L$ to $k = 1$, we obtain a *multiscale decomposition* of f^L into $(f^0, d^0, d^1, \dots, d^{L-1})$.

Two important classes of such decompositions are respectively associated to *point value* and *cell average* discretizations, which we describe here in the univariate setting for the sake of simplicity. In the first case, the f_i^k are viewed as the point values $f(2^{-k}i)$ of a function, so that the decimation operator is simply a downsampling according to $f_i^{k-1} = f_{2i}^k$. The prediction operator amounts to interpolating the odd values \tilde{f}_{2i+1}^k since by the consistency requirement, one has $\tilde{f}_{2i}^k = f_i^{k-1}$. In the second case, they are viewed as cell averages $2^k \int_{2^{-k}i}^{2^{-k}(i+1)} f(t) dt$ of a function, so that the decimation operator is defined by the half sum $f_i^{k-1} = \frac{1}{2}(f_{2i}^k + f_{2i+1}^k)$. The prediction operator “interpolates” these averages since by the consistency requirement, one has $\tilde{f}_{2i}^k + \tilde{f}_{2i+1}^k = 2f_i^{k-1}$. In both cases, the details can thus be simply defined by the prediction error at the odd samples, i.e., $d_i^{k-1} = f_{2i+1}^k - \tilde{f}_{2i+1}^k$.

When dealing with discrete data coming from a piecewise smooth function, the discretization by point values might not be well defined, especially at jump discontinuities. On the other hand, the discretization by cell averages acts naturally on the space of integrable functions and it provides a more adequate setting to deal with piecewise smooth signals, such as geometric images. Because of this, we shall carry out our numerical study within the cell average framework.

In this context, a classical prediction technique is to first construct on each interval $[2^{-k+1}i, 2^{-k+1}(i+1)]$ a polynomial p_i which interpolates the cell averages on some stencil $S = \{2^{-k+1}(i-A), 2^{-k+1}(i+B+1)\}$ containing this interval ($A, B > 0$), i.e., such that

$$2^{k-1} \int_{2^{-k+1}j}^{2^{-k+1}(j+1)} p_i = f_j^{k-1}, \quad j = i-A, \dots, i+B. \quad (2.2)$$

The predicted values are then defined by the averages of p_i on the half-intervals, i.e.,

$$\tilde{f}_{2i}^k = 2^k \int_{2^{-k}2i}^{2^{-k}(2i+1)} p_i \quad \text{and} \quad \tilde{f}_{2i+1}^k = 2^k \int_{2^{-k}(2i+1)}^{2^{-k}(2i+2)} p_i.$$

If we use polynomials of degree $2M$ and centered stencils $\{2^{-k+1}(i-M), 2^{-k+1}(i+M+1)\}$ for some fixed integer $M > 0$, we obtain a linear prediction scheme, and the multiresolution decomposition is then equivalent to a biorthogonal wavelet transform for which the dual scaling function is the box function $\bar{\varphi} = \chi_{[0,1]}$ (see [5]). The number M reflects the order accuracy $2M+1$ of the prediction scheme. While raising M improves

the accuracy in the smooth regions, it enlarges the stencil and thus increases the spreading of the prediction error near the edges, i.e., the number of important detail coefficients.

Nonlinear methods aim to reduce this problem. A strategy, introduced first in [15], is to consider an *essentially nonoscillatory* (ENO) reconstruction. The idea is to reconstruct several polynomials p_i^m of degree $2M$, associated with the stencils $\{2^{-k+1}(i - m), 2^{-k+1}(i + 2M + 1 - m)\}$, $m = 0, \dots, 2M$, and to select the polynomial p_i within this set in order to minimize the effect of the singularities on the loss of accuracy. The stencil selection process uses the divided differences of the discrete set to be interpolated as smoothness indicators: large divided differences indicate a possible loss of smoothness within the stencil. The selected stencils tend to “escape” from large gradients and singularities, so that the high-order accuracy is lost only within the intervals $[2^{-k+1}i, 2^{-k+1}(i + 1)]$ that contain the singularities.

A more refined strategy, introduced in [11], improves on ENO reconstruction within such intervals by *subcell resolution* (ENO–SR). The idea is to apply a *singularity detection* mechanism on the data f_i^{k-1} and to use these data in order to precisely localize the position x of potential jumps within the interval $[2^{-k+1}i, 2^{-k+1}(i + 1)]$ where detection occurred. Then, in place of a single polynomial p_i , we use on this interval p_i^l for $t \leq x$ and p_i^r for $t \geq x$, respectively reconstructed from the stencils $\{2^{-k+1}(i - 2M - 1), 2^{-k+1}(i)\}$ and $\{2^{-k+1}(i + 1), 2^{-k+1}(i + 2M + 2)\}$.

For more details on the mechanisms of stencil selection, singularity detection, and localization, we refer to [2]. See also [3] for a class of nonlinear multiscale representations based on the so-called *lifting scheme*. In all our subsequent numerical experiments, we use third-order accurate prediction schemes based on quadratic polynomial reconstruction (linear, ENO, ENO–SR), i.e., $M = 2$, and we apply the usual *tensor product* multiscale decomposition methods in order to extend the above described techniques to images.

3. ERROR CONTROL

The multiresolution decompositions based on ENO and ENO–SR predictions are nonlinearly data dependent and cannot be thought of as a decomposition in a wavelet basis, although closely related. This brings out new difficulties when it comes to nonlinear approximation by thresholding procedures. In the linear context it is natural thresholding procedures of the type

$$d_j^k \mapsto \hat{d}_j^k = \text{tr}(d_j^k; \varepsilon_k) = \begin{cases} 0 & |d_j^k| \leq \varepsilon_k \\ d_j^k & \text{otherwise,} \end{cases} \quad (3.1)$$

where the threshold ε_k might vary with scale depending on the norm that one wishes to control ($\varepsilon_k = \varepsilon 2^{kd/p}$ for L^p in d -dimensions). In the nonlinear context, however, there is no clear evidence that such a procedure results in a stable perturbation on the reconstructed signal and no simple way of estimating the approximation error from the size of the discarded coefficients. In particular, reconstruction from the thresholded coefficients might result in selecting different stencils than with the full decomposition.

The *error control algorithm*, introduced in [12], provides an alternative approach to nonlinear approximation in which a prescribed approximation accuracy is ensured by *intertwining* the decomposition and thresholding process. Roughly speaking, the algorithm computes nonlinear approximations \hat{f}^k of the data f^k from coarse to fine levels

$k = 0, \dots, L$ in the following way: at the coarsest level $k = 0$, we simply define $\hat{f}^0 = f^0$. Then for $k = 0, \dots, L - 1$, we compute a modified \tilde{f}^{k+1} by applying the prediction operator on \hat{f}^k , and we derive the details d^k from the prediction error $\tilde{f}^{k+1} - \hat{f}^{k+1}$. We then apply (3.1) to obtain \hat{d}^k and we define \hat{f}^{k+1} at the next level by reconstructing from \hat{f}^k and \hat{d}^k . Observe that the value of the details depends on the thresholding error at coarser levels. With such a modified algorithm, it is then possible to control the resulting error at the finest scale in various norms. In our numerical experiments, we shall use the quantities

$$\begin{aligned} \|f^L\|_\infty &= \sup_i |f_i^L| & \|f^L\|_1 &= \frac{1}{N_L} \left(\sum_i |f_i^L| \right) \\ \|f^L\|_2^2 &= \frac{1}{N_L} \left(\sum_i |f_i^L|^2 \right), \end{aligned} \quad (3.2)$$

where $N_L = 2^{2L}$ is the number of pixels in the image, and the L^2 -normalized thresholding strategy $\varepsilon_k = \varepsilon 2^{k-L}$. It is proven in [1] that with such a strategy, the error control algorithm always guarantees the estimates

$$\|\tilde{f}^L - \hat{f}^L\|_\infty \leq 2\varepsilon, \quad \|\tilde{f}^L - \hat{f}^L\|_1 \leq \varepsilon, \quad \|\tilde{f}^L - \hat{f}^L\|_2 \leq \varepsilon. \quad (3.3)$$

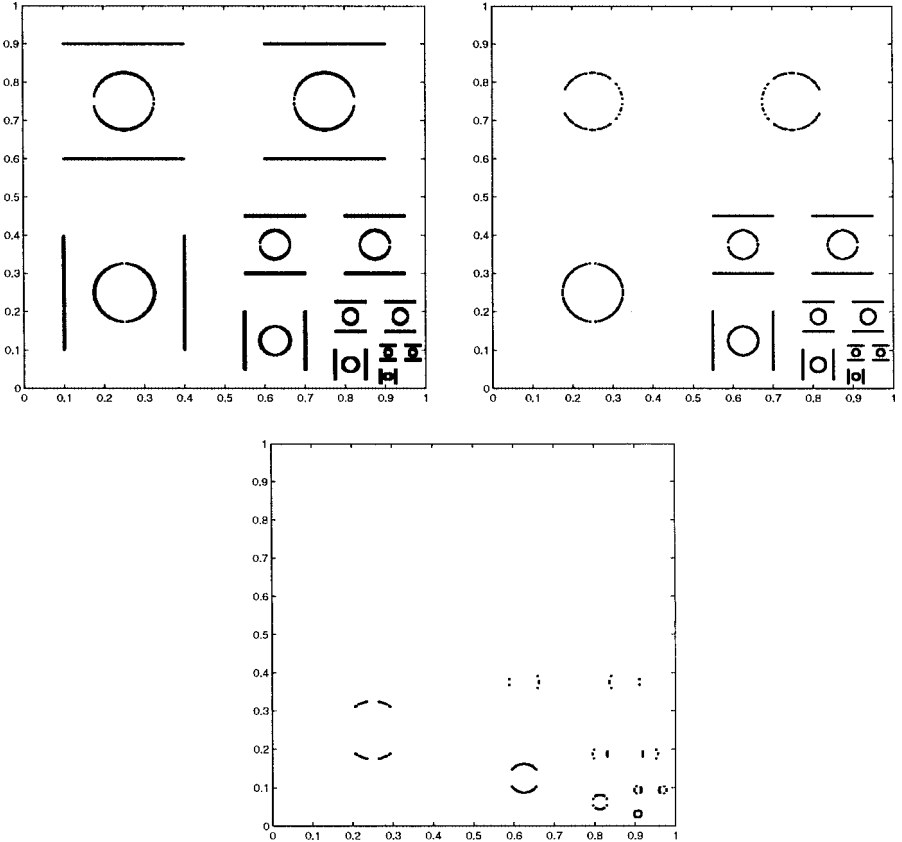


FIG. 1. Geometrical figure. Location (and total number) of nonzero scale coefficients in the multiresolution representation. Left: BOW (6840), right: ENO (1668), and bottom: ENO-SR (236).

TABLE 1
Data Compression with ENO Schemes

	Step	$\ \cdot \ _\infty$	$\ \cdot \ _1$	$\ \cdot \ _2$	nnz
$\varepsilon = 45$	LIN	54.2	0.700	2.36	2200
	ENO	48.2	0.0567	0.703	1504
	SR	42.8	0.0352	0.788	182
$\varepsilon = 18.7$	LIN	18.1	0.106	0.711	6024

These estimates are based on considering the worst case, where all the thresholded details at level k have absolute value ε_k . They are not therefore expected to be sharp, especially for the L^1 and L^2 error, which are in practice much smaller. On the other hand, the choice of an L^2 -normalized threshold is expected to produce the best asymptotic behavior of the L^2 norm with respect to the number of preserved coefficients.

4. NUMERICAL EXPERIMENTS

In this numerical study we shall consider three different types of two-dimensional images:

- A synthetic geometrical image: a circle and a square at different gray levels.

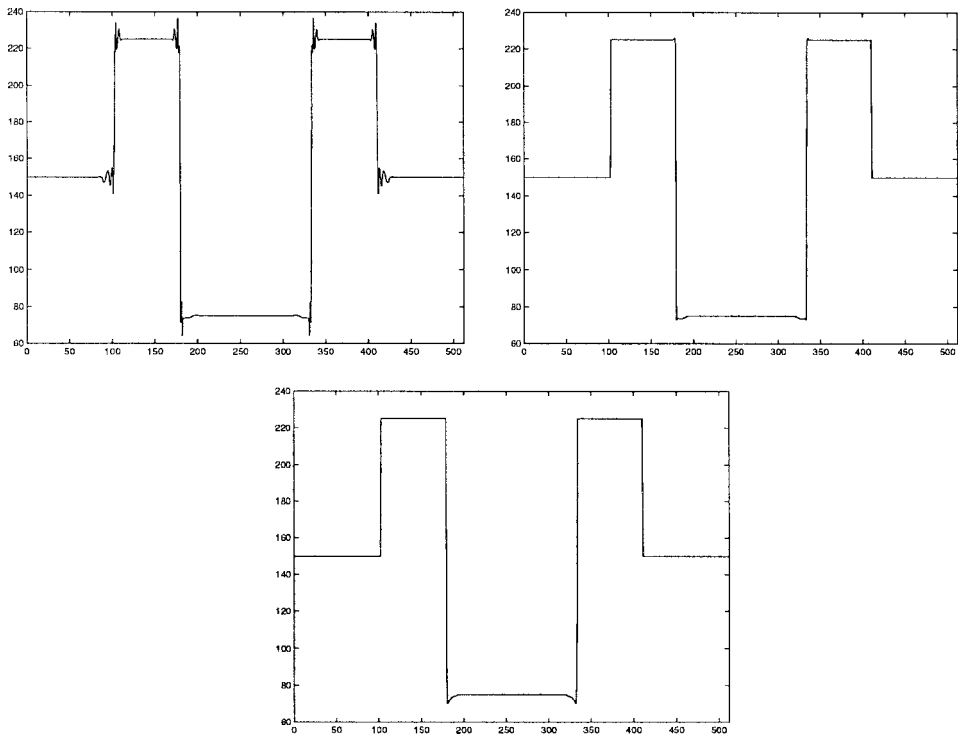


FIG. 2. Geometrical figure. $\varepsilon = 45$. Horizontal cuts of the reconstructed figures. Left: BOW, right: ENO, and bottom: ENO-SR.

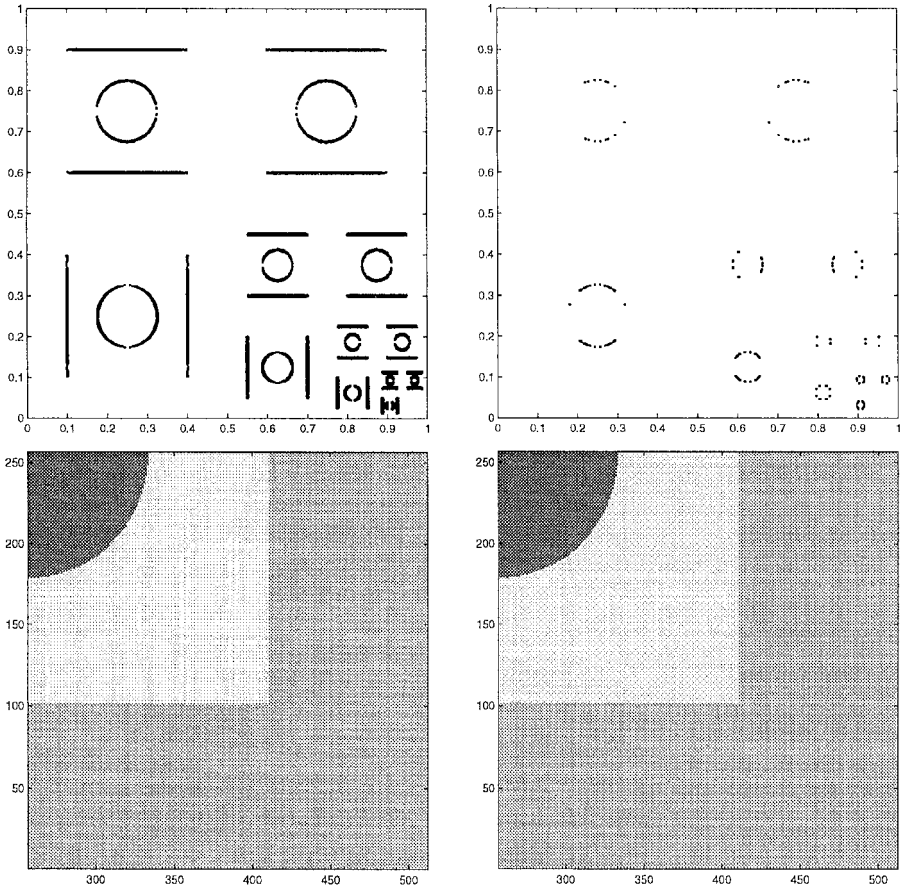


FIG. 3. Geometrical figure. Left: $\varepsilon = 18.7$, BOW scheme. Right: $\varepsilon = 45$, ENO-SR scheme. Top: location of nonzero scale coefficients. Bottom: reconstructed images from compressed representation.

- A piecewise smooth image: Harten's function (leftmost corner of Fig. 4; see [13] for the specification).
- A real image: Varda (leftmost corner of Fig. 9).

In all our numerical tests we take $L = 4$ and $N_L = 512 \times 512$. We consider third-order accurate prediction schemes. Each scheme is identified by an acronym:

- BOW: The biorthogonal wavelet (BOW) multiresolution scheme with $N = 1$ and $\bar{N} = 3$ in the notation of [7]. This scheme is equivalent to considering a four-point centered interpolation technique [2, 10, 14].
- ENO: The scheme obtained by considering a four-point ENO interpolatory technique.
- ENO-SR: The scheme obtained by considering a four-point ENO interpolatory technique with subcell resolution.

As mentioned in previous sections, BOW is a linear scheme, while ENO and ENO-SR are data-dependent nonlinear multiresolution schemes. Specific details on these nonlinear schemes and on our implementation can be found in [1, 2].

TABLE 2
Harten’s Function

	Step	$\ \cdot \ _\infty$	$\ \cdot \ _1$	$\ \cdot \ _2$	nnz
$\varepsilon = 1.2$	LIN	1.12	0.0271	0.0664	625
	ENO	1.27	0.0167	0.0557	473
	SR	1.34	0.0151	0.0546	370
$\varepsilon = 0.1$	LIN	0.115	0.0029	0.0062	8290
	ENO	0.094	0.0027	0.0045	2944
	SR	0.116	0.003	0.0057	1796

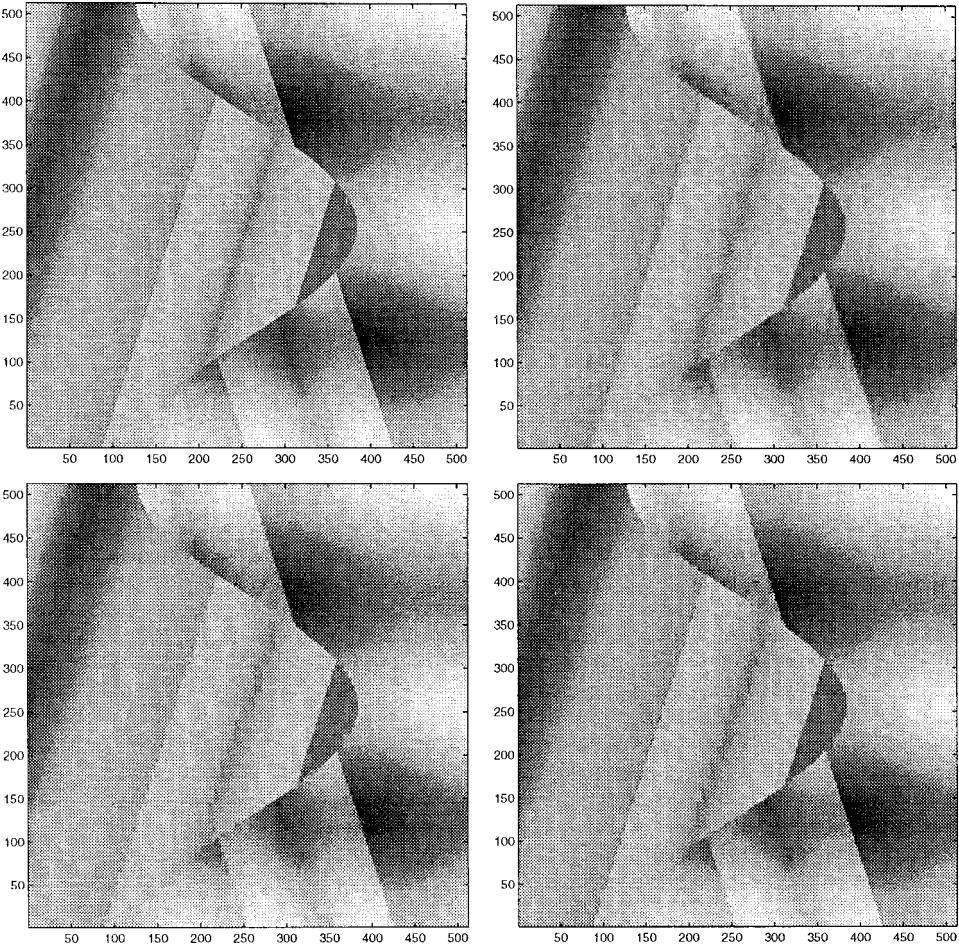


FIG. 4. Harten’s figure. Reconstruction with $\varepsilon = 1.2$. Top left: Original. Top right linear scheme. Bottom left: ENO. Bottom right: ENO–SR.

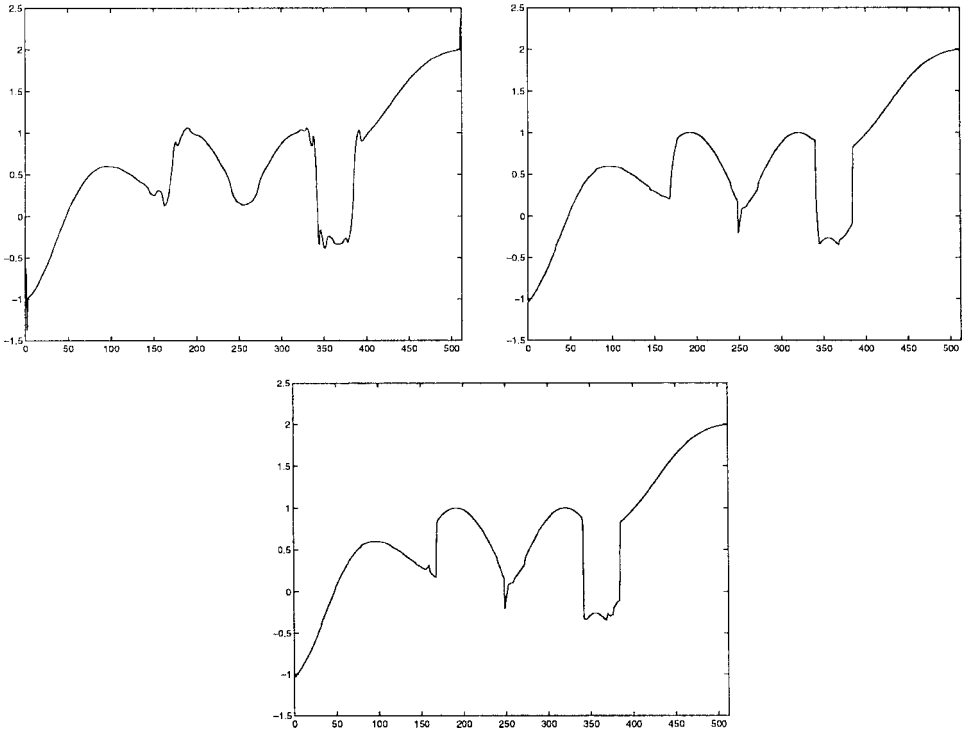


FIG. 5. Harten's figure. Horizontal cuts of the reconstruction with $\varepsilon = 1.2$. Top: Original and linear. Bottom: ENO and ENO-SR.

To ensure stability in the nonlinear case, we use the modified encoding algorithms described in [1, 2, 13] even for the linear scheme. In the linear case, this ensures that a prescribed accuracy is maintained. In the nonlinear case, it ensures, in addition, the stability of the inverse multiresolution transform with respect to perturbations.

Figure 1 displays the location of the nonzero scale coefficients in the *uncompressed* (i.e., no thresholding has been applied yet) multiresolution representation of the synthetic

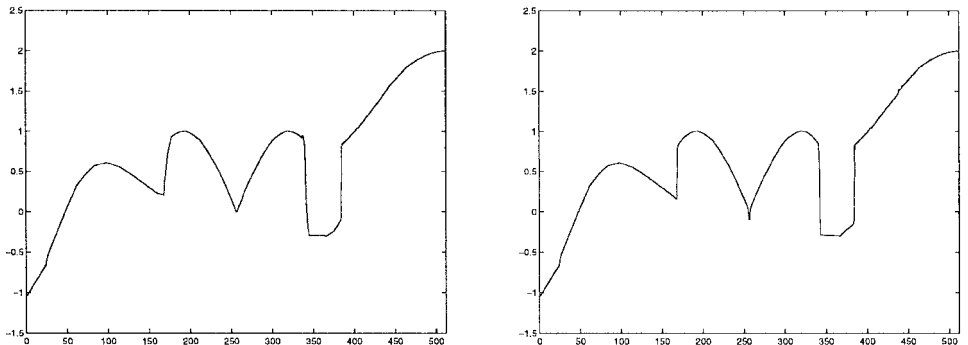


FIG. 6. Harten's figure. Horizontal cuts of the reconstruction with $\varepsilon = 1.2$ and the nonhierarchical choice of stencil. Left: ENO. Right: ENO-SR.

image under consideration:

$$u(x, y) = \begin{cases} 75 & (x - 0.5)^2 + (y - 0.5)^2 \leq 0.0225 \\ 225 & 0.2 \leq \max(|x|, |y|) \leq 0.8 \quad \& \quad (x - 0.5)^2 + (y - 0.5)^2 > 0.0225 \\ 150 & \text{else.} \end{cases} \tag{4.1}$$

The image is composed of flat regions separated by discontinuities, thus the nonzero coefficients pile-up in a neighborhood of the discontinuities. Notice that the number of nonzero scale coefficients for the BOW scheme is considerably larger than that for the ENO scheme (see [2]). It is worth noticing that the design principle of the ENO–SR technique makes this scheme into a kind of lossless compression technique for this particular type of signal.

Table 1 displays the number of nonzero scale coefficients in the compressed representation obtained when using a tolerance parameter $\varepsilon = 45$, as well as the actual error, computed in each one of the norms defined in (3.2).

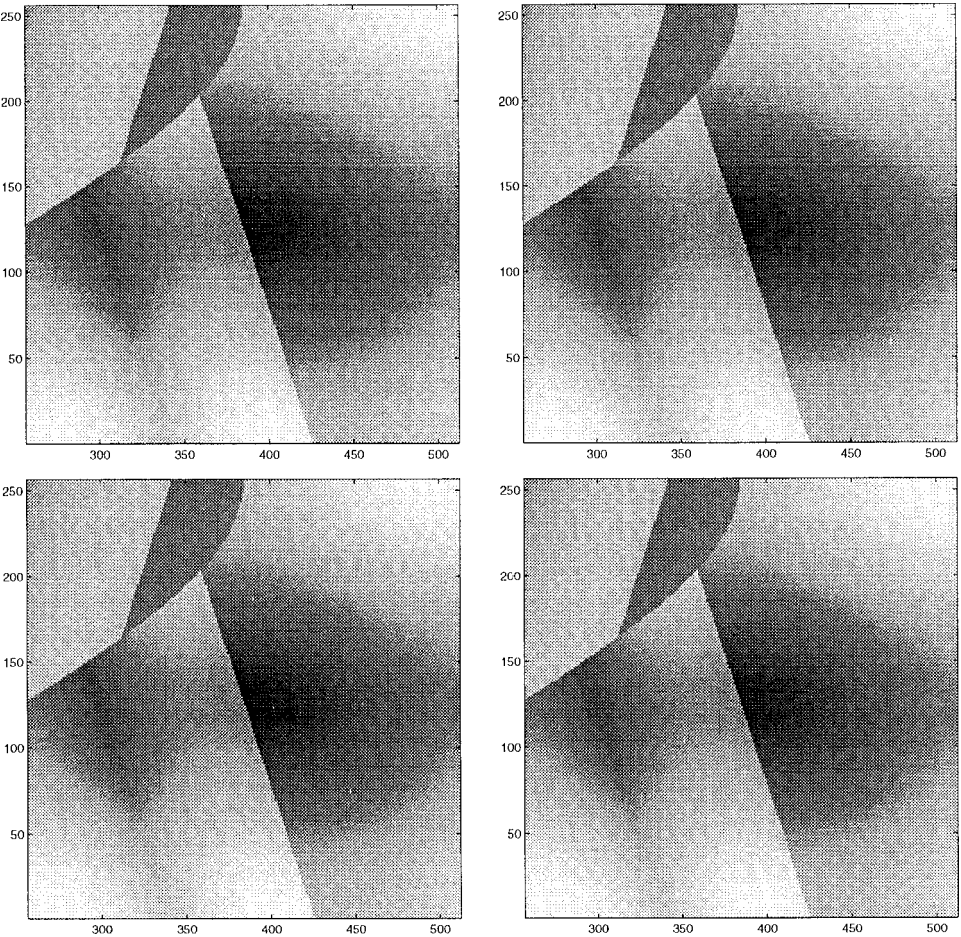


FIG. 7. Harten's figure. Partial reconstruction with $\varepsilon = 0.1$. Top: Original and linear. Bottom: ENO and ENO–SR.

The figures obtained from each one of the compressed multiresolution representations (not shown) are visually similar, and this is due to the fact that the 2-norm of the error is approximately of the same order in all three cases. The 2-norm of the error obtained with the BOW scheme is slightly larger, because there is a slight blurring of the discontinuities, due to the Gibbs-like phenomenon produced when using centered interpolatory techniques across discontinuities, which can be clearly appreciated in Fig. 2. For the sake of comparison we looked for a tolerance that would provide a similar error in the 2-norm for the linear scheme. The results are displayed for $\varepsilon = 18.7$ in Table 1 and also in Fig. 3.

The bottom portion of Fig. 3 displays a zoom of the bottom-right corner of the reconstructed data obtained with ENO–SR and $\varepsilon = 45$ and BOW with $\varepsilon = 18.7$. The error in the reconstructed image, measured in the 2-norm, is ≈ 0.7 in both cases. It can be observed that the quality is absolutely comparable, and it is remarkable that the small number of scale coefficients in the ENO–SR compressed representation lead in fact to a reconstructed figure of quality similar to that attained by the compressed representation obtained with the BOW scheme (with a number of coefficients larger by more than one order of magnitude: 182 versus 6024).

Our second test case, Harten’s 2D function, exhibits more complex behavior, although it is still composed of smooth portions separated by jumps and corners.

In Table 2 we show the number of nonzero scale coefficients as well as the errors in the different norms for each of the multiresolution-based compression schemes we

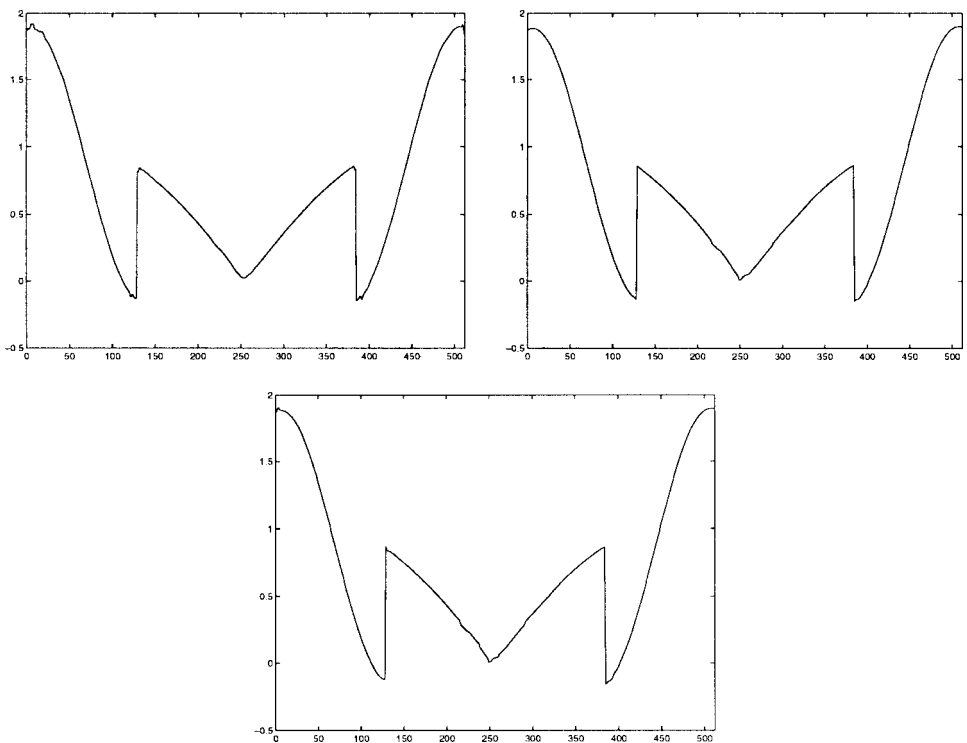


FIG. 8. Harten’s figure. Vertical cuts of the reconstructions with $\varepsilon = 0.1$. Top: Original and linear. Bottom: ENO and ENO–SR.

consider. The first portion of the table considers a fairly crude tolerance ($\varepsilon = 1.2$), to test the limitations of the schemes. As expected, the errors remain below the theoretical error bounds but it is probably more interesting to look at the reconstructed functions in Fig. 4. The linear scheme gives a smoothed out (and somewhat blurred) version of the original function, while the reconstructed figures obtained with the nonlinear schemes give sharper boundaries.

The difference in behavior can be appreciated in Fig. 5, where we observe again the Gibbs-like phenomenon typical of linear schemes in the presence of discontinuities. The nonlinear schemes keep sharp edges at discontinuities, but suffer from inaccuracies due to the roughness of the truncation strategy. It is worth mentioning here that we are using the *hierarchical* choice ([2] or references therein) of stencil in all our experiments. It is known (see, e.g., [2]) that the hierarchical choice might lead to inaccuracies around discontinuities in the second derivative. A corner in a function becomes a jump in the second derivative of its primitive; thus the hierarchical choice might lead to errors around corners when using the cell-average framework. To avoid this, we may want to use the *nonhierarchical* choice



FIG. 9. Varda's figure. Reconstruction with $\varepsilon = 45$. Top: Original and linear. Bottom: ENO and ENO-SR.

TABLE 3
Varda

	Step	$\ \cdot \ _\infty$	$\ \cdot \ _1$	$\ \cdot \ _2$	nnz
$\varepsilon = 45$	LIN	58.5	5.84	8.28	8438
	ENO	64.4	5.97	8.59	9648
	SR	63.8	6.04	8.68	10587

of stencil (see also [2] and references therein). Figure 6 is the equivalent to Fig. 5 but with a nonhierarchical ENO reconstruction.

The second part of Table 2 displays the results for a lower tolerance. At $\varepsilon = 0.1$, visual differences cannot be appreciated. Figure 7 displays a zoom of the bottom-right portion and Fig. 8 a vertical cut of the reconstructed function. It can be observed that we get essentially the same reconstructed function, but the nonlinear schemes, once again, are able to attain this with significantly less scale coefficients.

To end this study we consider a real image (Varda), the one depicted in the top left corner of Fig. 9.

Table 3 shows the relevant data for compression at $\varepsilon = 45$. We observe that the number of nonzero scale coefficients is comparable in all three cases, although slightly larger for the nonlinear schemes. The reconstructed images displayed in Fig. 9 show that the quality is also completely similar.

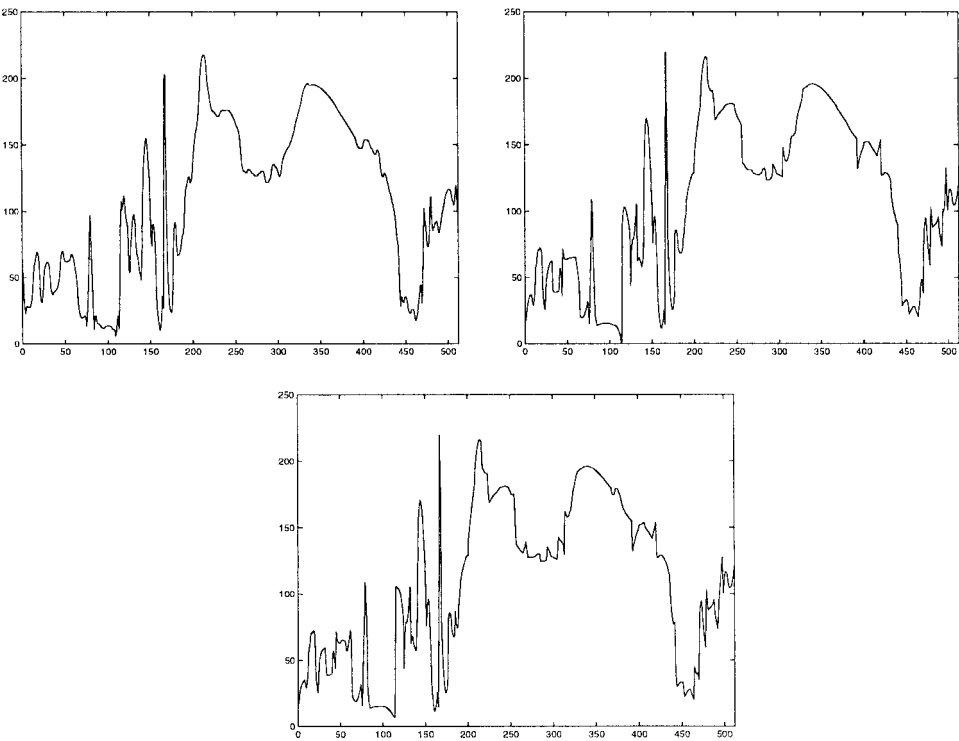


FIG. 10. Varda. Horizontal cuts of the reconstructions with $\varepsilon = 45$. Top: Original and linear. Bottom: ENO and ENO-SR.

Figure 10 shows horizontal cuts of the image and explains the poor behavior of ENO-based schemes: there are no clear regions of smoothness. An image is a noisy object, and divided differences, the essence of the ENO mechanism, are bad smoothness indicators in the presence of noise: Compression schemes whose basic design principle relies on piecewise polynomial interpolation techniques will have a poor performance when applied to noisy signals. Thus, ENO techniques, as described in this paper, do not produce a real gain, but they are no worse than linear techniques.

The last two sets of figures aim at quantifying the gain from using nonlinear techniques for the different 2D (two-dimensional) signals we consider.

In Fig. 11 we display the behavior of the L_2 -norm of the error with respect to the number of nonzero scale coefficients in the compressed representation. We clearly see that the behavior of the three compression schemes is very similar when applied to the real image; for a comparable number of nonzero scale coefficients we get a similar image (i.e., a similar error measured in the 2-norm). In the case of a piecewise smooth signal, there is a clear gain in efficiency when nonlinear schemes are used. Looking at the right and bottom graphs we see that the simpler the figure, the larger the gain.

Figure 12 shows the ratio between the nonzero scale coefficients in the compressed multiresolution representation for the linear BOW scheme and the nonlinear (ENO or ENO-SR) scheme versus the tolerance, for a range of tolerances $\varepsilon \approx 0$ to $\varepsilon \approx 0.5 * \|f\|$. Observe that the ratio is close to 1 (in fact slightly above 1) in the case of the real image,

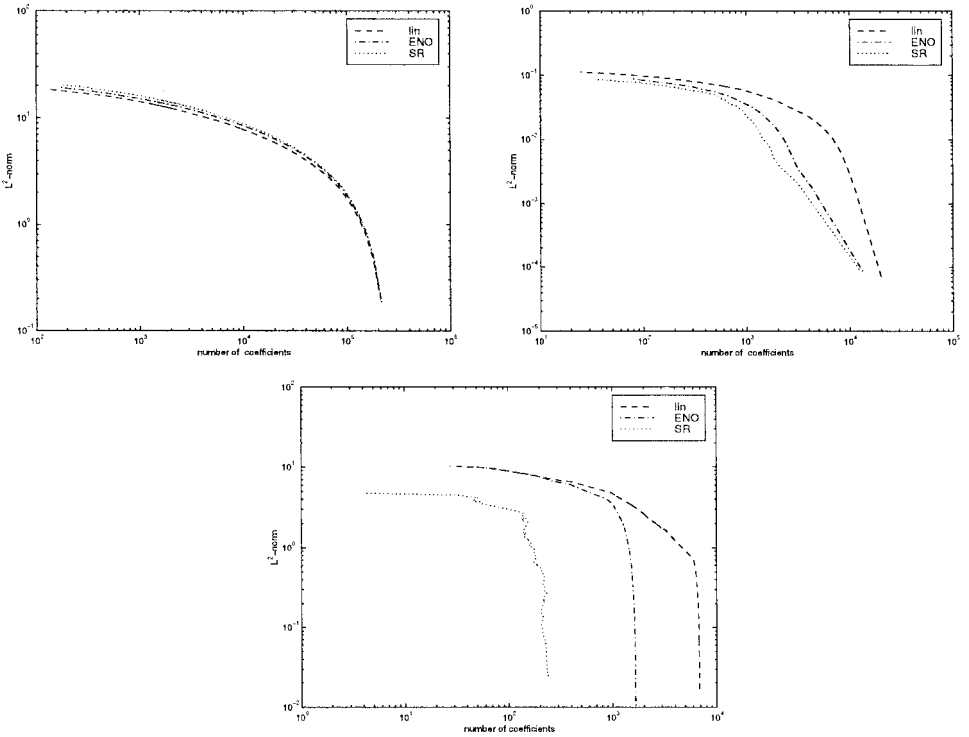


FIG. 11. $\|\hat{f}_L - \tilde{f}_L\|_2$ versus number of nonzero scale coefficients in \hat{f}_L . Left: Varda. Right: Harten's function. Bottom: Geometric figure.

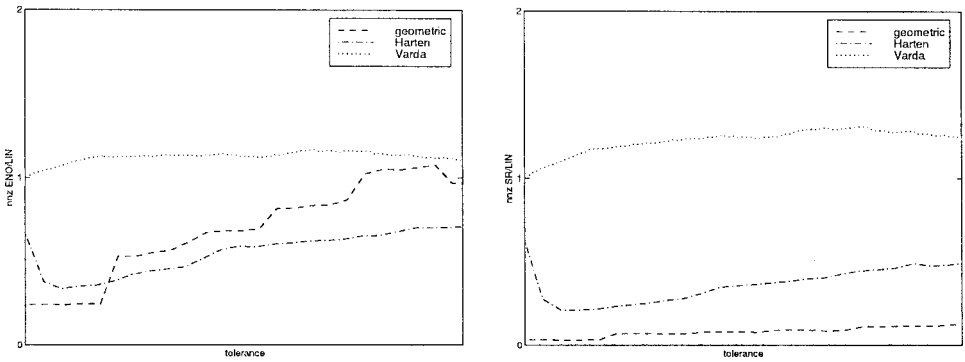


FIG. 12. Ratio between number of nonzero scale coefficients in multiresolution representation versus tolerance; Left: (ENO/linear), Right: (ENO-SR/linear); Geometric figure; Harten's function; Varda.

while it remains significantly below 1 for the smooth image and the geometric image at moderate tolerances. For very crude tolerances the ratio approaches one again in the case of the smooth image.

From Fig. 12, it is clear that these nonlinear techniques are most efficient for compression of piecewise smooth signals while keeping, at the same time, a moderate to high accuracy in the decompressed signal.

ACKNOWLEDGMENT

This work was initiated under the auspices of the CEMRACS project for applications of scientific computing (Marseille, summer 1998).

REFERENCES

1. S. Amat, F. Aràndiga, A. Cohen, and R. Donat, Tensor product multiresolution analysis with error control, Technical Report GrAN-99-4, Departament de Matemàtica Aplicada, University of València, submitted for publication.
2. F. Aràndiga and R. Donat, A class of nonlinear multiscale decompositions, Technical Report GrAN-99-1, Departament de Matemàtica Aplicada, University of València, *Numer. Algorithms* **23** (2000) 175–216.
3. R. L. Claypoole, G. Davis, W. Sweldens, and R. Baraniuk, Nonlinear wavelet transforms for image coding via lifting scheme, submitted for publication.
4. A. Cohen, W. Dahmen, I. Daubechies, and R. DeVore, Tree approximation and optimal encoding, Technical report, IGPM Report 174, RWTH-Aachen, 1999.
5. A. Cohen, I. Daubechies, and J. C. Feauveau, Biorthogonal bases of compactly supported wavelets, *Comm. Pure Appl. Math.* **45** (1992), 485–560.
6. A. Cohen, I. Daubechies, O. Guleryuz, and M. Orchard, On the importance of combining wavelet-based nonlinear approximation with coding strategies, *Appl. Comput. Harmon. Anal.*, in press.
7. I. Daubechies, “Ten Lectures on Wavelets,” CBMS-NSF Series in Applied Mathematics, No. 61, SIAM, Philadelphia, 1992.
8. R. DeVore, Nonlinear approximation, *Acta Numer.* (1997), 51–150.
9. F. Falzon and S. Mallat, Analysis of low bit rate image coding, *IEEE Trans. Signal Process.* **46** (1998), 1027–1042.

10. Murielle Guichaova, "Analyses Multirésolution Biorthogonales associées à la Résolution d'Equations aux Dérivées Partielles," Ph.D. thesis, Ecole Supérieure de Mécanique de Marseille, Université de la Méditerranée, Aix-Marseille II, 1999.
11. A. Harten, ENO schemes with subcell resolution, *J. Comput. Phys.* **83** (1989), 148–184.
12. A. Harten, Discrete multiresolution analysis and generalized wavelets, *J. Appl. Numer. Math.* **12** (1993), 153–193.
13. A. Harten, Multiresolution representation of cell-averaged data, Technical report, UCLA CAM Report 94-21, 1994.
14. A. Harten, Multiresolution representation of data. II. General framework, *SIAM J. Numer. Anal.* **33** (1996), 1205–1256.
15. A. Harten, B. Engquist, S. Osher, and S. Chakravarthy, Uniformly high order accurate essentially non-oscillatory schemes III, *J. Comput. Phys.* **71** (1987), 231–303.
16. A. Said and W. A. Pearlman, An image multiresolution representation for lossless and lossy compression, *IEEE Trans. Image Process.* **5**, No. 9 (1996), 1303–1310.
17. J. Shapiro, Embedded image coding using zero trees of wavelet coefficient, *IEEE Signal Process.* **41** (1993), 3445–3462.